

Synthetic Gauge Field for Ultracold Atoms Induced by Vector Beams

Huan Wang,^{1,2,3,*} Shangguo Zhu,^{1,2,3,4,*} Yun Long,^{1,2,3,4} Mingbo Pu,^{1,2,3,4} and Xiangang Luo^{1,2,4,†}

¹National Key Laboratory of Optical Field Manipulation Science and Technology,
Chinese Academy of Sciences, Chengdu 610209, China

²State Key Laboratory of Optical Technologies in Nano-Fabrication and Micro-Engineering,
Institute of Optics and Electronics, Chinese Academy of Sciences, Chengdu 610209, China

³Research Center on Vector Optical Fields, Institute of Optics and Electronics,
Chinese Academy of Sciences, Chengdu 610209, China

⁴College of Materials Science and Opto-Electronic Technology,
University of Chinese Academy of Sciences, Beijing 100049, China

(Dated: January 28, 2025)

Vector beams (VBs) with spatially varying polarization have broad applications across various fields of optics. We introduce a novel use of VBs to generate synthetic gauge fields for ultracold atoms. By leveraging VBs' rich tunability, this scheme enables the emergence of angular stripe phases over a significantly expanded parameter range, achieving a three-orders-of-magnitude enhancement in the phase diagram and thereby making experimental observation feasible. It also allows for the creation of topologically nontrivial giant skyrmions in spin space, with tunable topology controlled by VB parameters and without requiring rotation. Our work opens new avenues for utilizing VBs in quantum control of ultracold atoms and the exploration of exotic quantum states and phases.

Introduction.—Ultracold atoms provide exceptional controllability, making them an ideal platform for quantum simulation [1–3], quantum computation [4, 5], and quantum metrology [6]. A key direction is using ultracold atomic gases to simulate complex systems, including condensed matter models [7]. A significant milestone in this endeavor is the creation of synthetic gauge fields via engineered optical coupling between atomic internal states [8–12], particularly the realization of spin-orbit coupling (SOC) [10–18], an essential ingredient in many condensed matter systems such as topological insulators, superconductors, and semimetals [19–22]. This progress has enabled the realization of numerous complex quantum phenomena [23–36].

While synthetic SOC typically refers to the coupling between spins (atomic internal states, or pseudospins) and translational motion, spin-orbit-angular-momentum coupling (SOAMC)—a coupling between spins and rotational motion—has recently been proposed and realized in Bose-Einstein condensates (BECs) [37–42]. Unlike SOC, which uses Gaussian beams, SOAMC employs Laguerre-Gaussian beams (LGBs) carrying finite orbital angular momenta (OAM). Ultracold atomic systems with SOAMC are predicted to exhibit exotic quantum phases [43–46], most notably the angular stripe phase [47–52], which breaks $U(1)$ gauge symmetry and rotational symmetry, displaying supersolid-like behavior in the rotational degree of freedom. The angular stripe phase is confined to a tiny region of the phase diagram, making experimental observation challenging [39, 53, 54]. Reducing the waist of LGBs using a high-numerical-aperture (NA) lens has been proposed to enlarge this region [53, 54]. However, tightly focusing LGBs results in light fields lacking definite OAMs, thereby precluding SOAMC. A promising solution might lie in explor-

ing novel coupling schemes involving structured light fields [55], which provide greater flexibility for light field manipulation.

Vector beams, characterized by spatially nonuniform polarization, offer tunable degrees of freedom, including polarization state, orbital angular momentum, and beam shape [55–57]. These can be precisely controlled using spatial light modulators, phase plates and metasurfaces to create intricate vector light fields [56, 58–63], enabling novel applications [64], such as three-dimensional magnetic field measurement [65], and spatially dependent electromagnetically induced transparency [66].

In this Letter, we present a novel scheme to couple atomic pseudospins in a BEC using two VBs through a tightly focusing system, showcasing enhanced quantum control enabled by VBs' rich tunability. This setup generates a three-component synthetic magnetic field, contributing to SOAMC in the direction perpendicular to the applied magnetic field \mathbf{B} and a spatially dependent Zeeman shift along \mathbf{B} . First, we investigate the ground-state properties with only SOAMC and reveal an angular stripe phase with tunable discrete rotational symmetry, accessible over a significantly expanded experimental parameter range. This achieves a *three-orders-of-magnitude* enhancement in critical coupling strength compared to the conventional LGB scheme [39, 53], making experimental observation feasible. Next, incorporating both SOAMC and the spatially dependent Zeeman shift, we demonstrate a novel mechanism for generating stable multiply quantized vortices and topologically nontrivial giant skyrmions in spin space [67–72] with topology tunable via VB parameters and without requiring rotation. Finally, we discuss the realization of our scheme in current experiments.

Coupling scheme.—The time-independent electric field

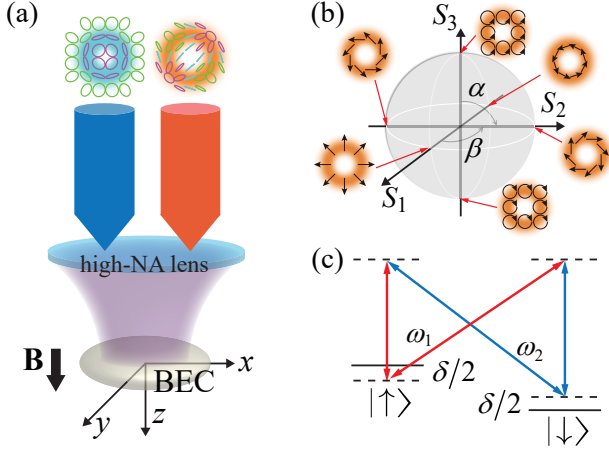


FIG. 1. (a) Illustration of two VBs passing through a tightly focusing system and illuminating a pancake-shaped BEC trapped near the focal plane ($z = 0$). Insets at the top display the polarization and amplitude distributions at the focal plane for VBs with $m_1 = 1$, $l_1 = 2$, $\alpha_1 = \pi/2$, $\beta_1 = 0$ (left) and $m_2 = 1$, $l_2 = 3$, $\alpha_2 = \pi/2$, $\beta_2 = 0$ (right) after focusing. Magenta, green, cyan represent left-handed elliptical, right-handed elliptical, and linear polarizations, respectively. (b) High-order Poincaré sphere for a VB (before focusing) with $m = 1$ and $l = 2$. S_1 , S_2 , and S_3 are the Stokes parameters [73]. Insets show polarization (black arrows) and amplitude (orange backgrounds) distributions for different α and β . (c) Atomic energy level structure with a double- Λ -type coupling scheme.

of a VB can be expressed as

$$\mathcal{E}(\rho, \varphi) = A_l(\rho, \varphi) \left[\cos(\alpha/2) e^{-i\beta/2} e^{-im\varphi} \hat{\mathbf{e}}_L + \sin(\alpha/2) e^{i\beta/2} e^{im\varphi} \hat{\mathbf{e}}_R \right], \quad (1)$$

where (ρ, φ, z) are cylindrical coordinates, with ρ and φ denoting the radius and azimuth angle, respectively, and the light propagates along the z -axis. The unit vectors $\hat{\mathbf{e}}_{L,R} \equiv (\hat{\mathbf{e}}_x \pm i\hat{\mathbf{e}}_y)/\sqrt{2}$ correspond to left (L) and right (R) circular polarization states. The amplitude $A_l(\rho, \varphi) = \sqrt{I}(\sqrt{2}\rho/w)^{|l|} e^{-\rho^2/w^2} e^{il\varphi}$ describes an LGB profile, where w is the beam waist, I is the light intensity, and l is the vortex topological charge. The combination of $e^{-im\varphi} \hat{\mathbf{e}}_L$ and $e^{im\varphi} \hat{\mathbf{e}}_R$ can be described by the high-order Poincaré sphere [73], with (α, β) as spherical coordinates ($0 \leq \alpha \leq \pi$, $0 \leq \beta \leq 2\pi$), as illustrated in Fig. 1 (b). The parameter m denotes the polarization topological charge.

Consider two VBs, labeled $j = 1, 2$, with optical frequencies ω_j and electric fields \mathcal{E}_j described by Eq. (1) with parameters $(m_j, l_j, \alpha_j, \beta_j)$. For simplicity, both VBs are assumed to have the same waist w . After passing through a high-NA lens, they form tightly focused VBs [74, 75], illuminating a pancake-shaped BEC near the focal plane, as shown in Fig. 1 (a). The tightly focused VBs exhibit three nonzero spatial components of their electric fields, $\mathbf{E}_j = (E_{xj}, E_{yj}, E_{zj})$ (explicit

forms detailed in the Supplemental Material (SM) [76]). These components are tunable via $(m_j, l_j, \alpha_j, \beta_j)$, offering great experimental flexibility to generate various light fields [56, 58–63]. An external Zeeman field \mathbf{B} is applied along the z -axis, inducing an energy splitting $\hbar\omega_Z$ between the two spin states $|\uparrow\rangle$ and $|\downarrow\rangle$, where $\hbar = h/2\pi$ is the reduced Planck constant. As shown in Fig. 1 (c), $|\uparrow\rangle$ and $|\downarrow\rangle$ are coupled through two-photon Raman transitions with detuning $\delta = \hbar(\omega_Z + \omega_1 - \omega_2)$, forming a double- Λ -type coupling scheme (see SM [76] for details).

When interatomic interactions are weak, the motion of atoms can be approximated as a two-dimensional problem [39, 45, 53, 54]. Here we focus on the physics at the focal plane. The system's dynamics and equilibrium properties are effectively governed by the Gross-Pitaevskii (GP) equation $i\hbar\partial_t\Psi = H\Psi$, where $\Psi = (\psi_\uparrow, \psi_\downarrow)^T$ is the spinor wave function of the BEC. The GP Hamiltonian is [76]

$$H = -\frac{\hbar^2\nabla_\rho^2}{2M} + \frac{1}{2}M\omega^2\rho^2 + V_S(\boldsymbol{\rho}) + V_{VB}(\boldsymbol{\rho}) + V_I(\boldsymbol{\rho}) + \frac{\delta}{2}\sigma_z, \quad (2)$$

where $\boldsymbol{\rho} \equiv (x, y)$ is the position in the $x-y$ plane, M is the atomic mass, ω is the transverse trapping frequency (with trap size $a_0 \equiv \sqrt{\hbar/M\omega}$), and $\vec{\sigma}_P \equiv (\sigma_x, \sigma_y, \sigma_z)$ represents the Pauli matrices. $V_S(\boldsymbol{\rho})$, $V_{VB}(\boldsymbol{\rho})$, and $V_I(\boldsymbol{\rho})$ are the potential induced by scalar light shift, the potential associated with the effective magnetic field induced by vector light shift, and the nonlinear mean-field interaction, respectively:

$$V_S(\boldsymbol{\rho}) = \Omega_s(\bar{\mathbf{E}}_1^* \cdot \bar{\mathbf{E}}_1 + \bar{\mathbf{E}}_2^* \cdot \bar{\mathbf{E}}_2), \quad (3)$$

$$V_{VB}(\boldsymbol{\rho}) = \begin{pmatrix} \Omega_z(\boldsymbol{\rho}) & \Omega_r(\boldsymbol{\rho}) \\ \Omega_r^*(\boldsymbol{\rho}) & -\Omega_z(\boldsymbol{\rho}) \end{pmatrix}, \quad (4)$$

$$V_I(\boldsymbol{\rho}) = \eta \begin{pmatrix} g_{\uparrow\uparrow}|\psi_\uparrow|^2 + g_{\uparrow\downarrow}|\psi_\downarrow|^2 & 0 \\ 0 & g_{\uparrow\downarrow}|\psi_\uparrow|^2 + g_{\downarrow\downarrow}|\psi_\downarrow|^2 \end{pmatrix}. \quad (5)$$

Here $\bar{\mathbf{E}}_j \equiv \mathbf{E}_j/\sqrt{I_j} \equiv (\bar{E}_{xj}, \bar{E}_{yj}, \bar{E}_{zj})$ with I_j the light intensity. The off-diagonal term of V_{VB} , $\Omega_r(\boldsymbol{\rho}) = \Omega_0[(\bar{E}_{z2}^* \bar{E}_{x1} - \bar{E}_{x2}^* \bar{E}_{z1}) + i(\bar{E}_{y2}^* \bar{E}_{z1} - \bar{E}_{z2}^* \bar{E}_{y1})]$, drives transitions between Zeeman sublevels, coupling spin and OAM. The diagonal term of V_{VB} , $\Omega_z(\boldsymbol{\rho}) = i\Omega_0(\bar{E}_{x1}^* \bar{E}_{y1} - \bar{E}_{y1}^* \bar{E}_{x1} + \bar{E}_{x2}^* \bar{E}_{y2} - \bar{E}_{y2}^* \bar{E}_{x2})$, absent in LGB-induced SOAMC schemes [37–42], introduces a spatially dependent Zeeman shift, providing additional control. The interaction strength $g_{\sigma\sigma'} = 4\pi\hbar^2 N a_{\sigma\sigma'}/M$, where $a_{\sigma\sigma'}$ is the s-wave scattering length between spins $\sigma = \uparrow, \downarrow$, and N is the atom number. The parameter $\eta = 1/(\sqrt{2}\pi a_0 z)$ is a dimensional reduction factor, with $a_0 z$ representing the atom cloud width along the z -axis [76].

Angular stripe phase.—The multiple tunable degrees of freedom in VBs allow for various outcomes based on the Hamiltonian H in Eq. (2) for different VB combinations. For simplicity, we consider the case $m_1 = m_2 = 1$ and $l_1 = -l_2 = n$, where n is a tunable integer (other parameter choices are discussed in the SM [76]). Without loss of

generality, we set $\alpha_1 = \alpha_2 = \pi/2$ and $\beta_1 = \beta_2 = 0$. Under this configuration, $V_{\text{VB}}(\boldsymbol{\rho})$ contains only the off-diagonal term, with elements given by [76]

$$\Omega_z = 0, \quad \Omega_r = \Omega_0 f(\rho) e^{i\Delta l \varphi}, \quad (6)$$

where $f(\rho)$ describes the spatial distribution and $\Delta l = l_1 - l_2 - 1 = 2n - 1$ represents the OAM transfer during the Raman process.

We first focus on single-particle physics, neglecting interatomic interactions. Defining two OAMs $n_\uparrow \equiv n - 1$ and $n_\downarrow \equiv -n$, we transform the basis states as $\psi_\sigma \rightarrow e^{in_\sigma \varphi} \psi_\sigma$. Substituting into Eq. (2), the single-particle Hamiltonian becomes

$$H_0 = -\frac{\hbar^2}{2M} \frac{1}{\rho} \frac{\partial}{\partial \rho} \left(\rho \frac{\partial}{\partial \rho} \right) + \frac{L_z^2}{2M\rho^2} + \frac{1}{2} M\omega^2 \rho^2 + V_S(\rho) + \frac{\hbar\gamma}{M\rho^2} L_z + \frac{\hbar^2 \gamma^2}{2M\rho^2} + \frac{\delta}{2} \sigma_z + \Omega_r(\rho) \sigma_x, \quad (7)$$

where $L_z = -i\hbar \partial_\varphi$ is the quasiangular momentum (QAM) operator, and $\gamma = \frac{n_\uparrow + n_\downarrow}{2} + \frac{n_\uparrow - n_\downarrow}{2} \sigma_z$ is a scaling matrix. Since $[L_z, H_0] = 0$, each eigenstate has a definite QAM l_z , which is related to the OAM m_σ of spin component σ in the laboratory frame via $m_\sigma = l_z + n_\sigma$. The term $\hbar\gamma L_z / M\rho^2$ introduces coupling between spin and OAM when $n_\uparrow \neq n_\downarrow$. Due to rotational symmetry, the wave function can be expressed as $\psi_\sigma(\boldsymbol{\rho}) = \tilde{f}_{\sigma\tilde{n}}(\rho) e^{il_z \varphi} / \sqrt{2\pi}$, where \tilde{n} is the radial quantum number. We solve $H_0 \Psi = E \Psi$ to obtain the single-particle energy spectrum [45, 48] (Fig. 2 (a)). By varying Ω_0 and δ , we compute the single-particle phase diagram (Fig. 2 (b)) using imaginary time evolution [77, 78].

At zero detuning δ and small coupling strength Ω_0 , the ground state typically exhibits twofold degeneracy at $l_z = -n_\uparrow$ and $l_z = -n_\downarrow$, as seen in the middle panel of Fig. 2 (a). The density modulation can be described by [50]

$$|\psi_\uparrow|^2 = |\psi_\downarrow|^2 = \bar{n}_0(\rho) \left\{ \frac{1}{2} + \frac{1}{2} \bar{n}_1(\rho) \cos[\Delta l \varphi + \bar{\varphi}] \right\}, \quad (8)$$

where $\bar{n}_0(\rho)$ is the azimuthally averaged density, satisfying $\int d\rho 2\pi\rho \bar{n}_0(\rho) = N$, $\bar{n}_1(\rho)$ is the modulation contrast, and $\bar{\varphi}$ is a phase constant. This describes an azimuthal density modulation with a period of $2\pi/\Delta l$, forming an angular stripe phase. Consistent with our numerical results, the angular stripe phase exhibits a discrete $(2n-1)$ -fold rotational symmetry, as shown in the inset (point B) of Fig. 2 (b).

For nonzero detuning δ , the ground-state degeneracy is lifted, and the ground-state energy localizes at a single minimum, as shown in the left and right panels of Fig. 2 (a). At $\delta < 0$, increasing Ω_0 from 0, the phase diagram splits into regions with ground-state QAM $l_z = -n_\uparrow, -n_\uparrow + 1, \dots$, corresponding to OAM $(m_\uparrow, m_\downarrow) = (0, -2n + 1), (1, -2n + 2), \dots$. At $\delta > 0$, increasing Ω_0 from 0, the phase diagram splits into regions

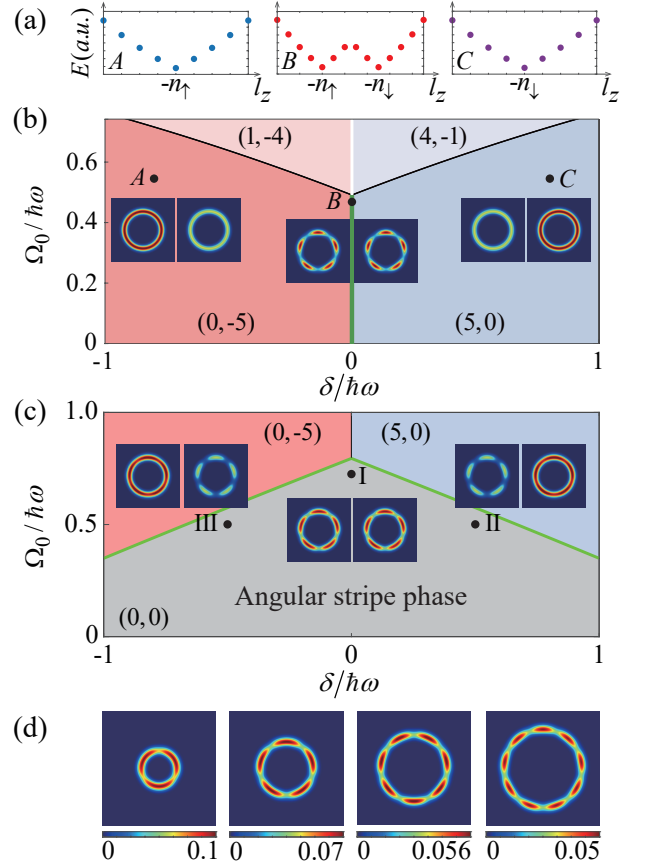


FIG. 2. (a) Single-particle energy spectra corresponding to points A (left), B (middle), and C (right) in (b). (b) Single-particle phase diagram in the $\Omega_0 - \delta$ plane for $n = 3$ and $\Omega_s/\hbar\omega = -13$. Phases are labeled by $(m_\uparrow, m_\downarrow)$. The green solid line represents the angular stripe phase for $\delta = 0$ and $0 \leq \Omega_0 \leq \Omega_0^c$, where $\Omega_0^c \approx 0.48\hbar\omega$. Insets show normalized density distributions $|\psi_\sigma|^2 a_0^2/N$ (left for $\sigma = \uparrow$, right for $\sigma = \downarrow$) at points A, B, and C, with $(\delta, \Omega_0)/\hbar\omega = (-0.8, 0.55)$, $(0, 0.47)$, and $(0.8, 0.55)$, respectively. The spin \downarrow density distribution at A and \uparrow at C are magnified 10 times for viewing. (c) Phase diagram for weakly interacting BECs with scattering lengths $a_{\uparrow\uparrow} = a_{\downarrow\downarrow} = 45a_B$ and $a_{\uparrow\downarrow} = 0.5a_{\uparrow\uparrow}$, where a_B is the Bohr radius. Other parameters are the same as in (b). The angular stripe phase (gray) achieves a critical coupling strength $\Omega_0^c \approx 0.82\hbar\omega$ at $\delta = 0$. Insets show normalized density distributions of the angular stripe phase at points I, II, and III, with $(\delta, \Omega_0)/\hbar\omega = (0, 0.75)$, $(0.5, 0.5)$, and $(-0.5, 0.5)$, respectively. (d) Angular stripe phases with varying periodicity. $|\psi_\uparrow|^2 a_0^2/N$ are shown for $x, y \in [-5a_0, 5a_0]$, at $\delta = 0$ and the following parameters: (left) $n = 2$, $\Omega_s/\hbar\omega = -29.27$, $\Omega_0/\hbar\omega = 1.63$; (middle left) $n = 3$, $\Omega_s/\hbar\omega = -13$, $\Omega_0/\hbar\omega = 0.75$ (same as point I in (c)); (middle right) $n = 4$, $\Omega_s/\hbar\omega = -3.9$, $\Omega_0/\hbar\omega = 0.2$; (right) $n = 5$, $\Omega_s/\hbar\omega = -0.85$, $\Omega_0/\hbar\omega = 0.04$.

with $l_z = -n_\downarrow, -n_\downarrow - 1, \dots$, corresponding to $(m_\uparrow, m_\downarrow) = (2n-1, 0), (2n-2, -1), \dots$. These ground states correspond to spin-polarized phases without azimuthal density modulation, as illustrated in the insets (points A and C) of Fig. 2 (b).

Now we examine the phase diagram with weak inter-

atomic interactions, focusing on the case $g_{\uparrow\uparrow} > g_{\uparrow\downarrow}$, which favors a balanced density profile between spin components. Using the imaginary time evolution method [77, 78], we obtain the ground-state phase diagram shown in Fig. 2 (c). Compared to the single-particle case, interactions alter the phase boundaries. The angular stripe phase with $(m_{\uparrow}, m_{\downarrow}) = (0, 0)$ expands from a line into a broader region, as interactions serve as a stabilizing factor against detuning, thereby extending its parameter range. For $\delta = 0$, the system exhibits a spin-balanced angular stripe phase, while for $\delta \neq 0$, it transitions to a spin-imbalanced angular stripe phase, absent in the single-particle scenario. Increasing the coupling strength Ω_0 beyond a critical value Ω_0^c leads to spin-polarized phases, with $(m_{\uparrow}, m_{\downarrow}) = (0, -2n+1)$ for $\delta < 0$, or $(m_{\uparrow}, m_{\downarrow}) = (2n-1, 0)$ for $\delta > 0$, both without azimuthal density modulation.

Enabled by the rich tunability of VBs, the angular stripe phase exhibits tunable $C_{\Delta l}$ discrete rotational symmetry, where $\Delta l = 2n - 1$ and n is controlled by VB parameters. By varying n , angular stripe phases with arbitrary odd periodicities can be achieved. As shown in Fig. 2 (d), C_3, C_5, C_7 , and C_9 rotational symmetries can be achieved by selecting appropriate values of n, Ω_s , and Ω_0 , while keeping other parameters consistent with Fig. 2 (c). As n increases, the ring size of the angular stripe phase grows, while the required coupling strength Ω_0 decreases, indicating a shrinking phase diagram region and a narrower experimental parameter window. Therefore, smaller n values would be more experimentally feasible.

Spin texture.—Our coupling scheme with VBs can generate exotic spin textures. The potential $V_{\text{VB}}(\boldsymbol{\rho})$ can include both nonzero Ω_r and Ω_z in Eq. (4), whereas Ω_z is absent in LGB-induced SOAMC. For parameters $\beta_1 = \beta_2 = 0, m_1 = m_2 = 1, l_1 = 2$, and $l_2 = -4$, the elements of $V_{\text{VB}}(\boldsymbol{\rho})$ become [76]

$$\Omega_z = \Omega_0 f_z(\rho), \quad \Omega_r = \Omega_0 f(\rho) e^{i\Delta l \varphi}, \quad (9)$$

where $f_z(\rho)$ and $f(\rho)$ describe the spatial distributions, and the OAM transfer $\Delta l = l_1 - l_2 - 1 = 5$. For simplicity, we set $\Omega_s = 0$, achievable by choosing the tune-out wavelength. The GP equation with vanishing interaction is solved for various α_1 and α_2 to analyze the ground-state spin textures.

The ground-state spin texture is described by the spin density vector $\mathbf{S} = \Psi^\dagger \boldsymbol{\sigma}_P \Psi / |\Psi|^2$. For $\alpha_1 = \alpha_2 = 0.37\pi$, and $\alpha_1 = \alpha_2 = 0.45\pi$, S_x, S_z , and \mathbf{S} are shown in Fig. 3 (a) (c) and (b) (d), respectively (see SM [76] for details on density profiles and relative phases). Both S_x and S_y exhibit periodic modulation in the azimuthal direction, with a periodicity determined by Δl , similar to the angular stripe phase.

The ground state exhibits a stable multiply quantized vortex with its quantized circulation determined by Δl [76]. For $\alpha_1 = \alpha_2 = 0.37\pi$, it forms two topological giant skyrmions in spin space [67–72], while for

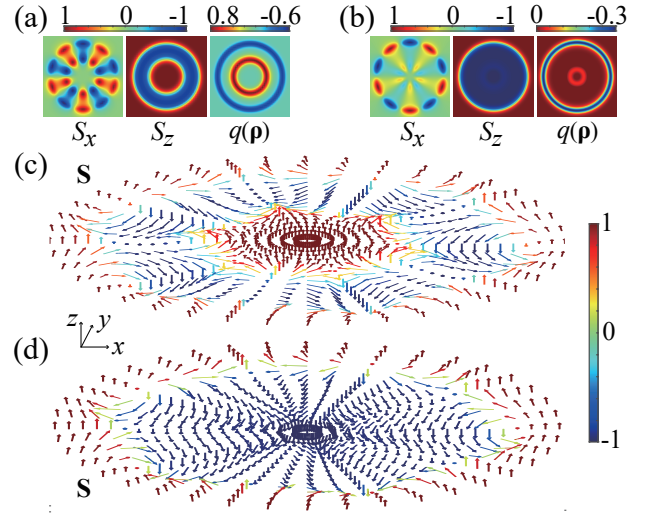


FIG. 3. Spin textures and topological charge densities. (a) and (c) correspond to $\alpha_1 = \alpha_2 = 0.37\pi$, while (b) and (d) correspond to $\alpha_1 = \alpha_2 = 0.45\pi$. In (a) and (b), the left, middle, and right panels display S_x, S_z , and $q(\boldsymbol{\rho})$, respectively, with spatial ranges $x, y \in [-3.5a_0, 3.5a_0]$ in (a) and $x, y \in [-5a_0, 5a_0]$ in (b). In (c) and (d), arrows indicate the distribution of \mathbf{S} , and the color bar represents S_z .

$\alpha_1 = \alpha_2 = 0.45\pi$, there is one. Along the radial direction, \mathbf{S} flips from north to south (or vice versa) when crossing the annular giant skyrmions. These topological structures are characterized by the topological charge density $q(\boldsymbol{\rho})$ (right panels of Fig. 3 (a) and (b)) and the topological charge Q [79], defined as

$$q(\boldsymbol{\rho}) = \mathbf{S} \cdot (\partial_x \mathbf{S} \times \partial_y \mathbf{S}) / 4\pi, \quad Q = \int_{\mathcal{A}} d^2\rho q(\boldsymbol{\rho}), \quad (10)$$

where \mathcal{A} is the annular region $\rho_1 < \rho < \rho_2$ enclosing the skyrmion of interest. At $\alpha_1 = \alpha_2 = 0.37\pi$, the inner ring has topological charge $Q_{\text{in}} = 5$ and the outer ring $Q_{\text{out}} = -5$. Increasing α_1 and α_2 to $\alpha_1 = \alpha_2 = 0.45\pi$ alters the spatial distribution of Ω_z , reversing the spin imbalance in the inner region [76], and resulting in a single skyrmion with topological charge $Q = -5$. The absolute values of the topological charges are determined by Δl . Previously, generating such giant skyrmions required adding rotations [67–69, 71]. In contrast, our scheme provides a novel approach to create giant skyrmions without rotation, and with their topology tunable via VB parameters.

Experiment observation.—In conventional LGB-induced SOAMC systems, the angular stripe phase occupies a tiny region in the phase diagram, with a critical coupling strength $\Omega_0^c \approx h \times 0.0155\text{Hz}$ [39, 53] at $\delta = 0$, which is nearly unattainable experimentally [53, 54]. While reducing the LGB waist using a high-NA lens has been proposed to expand this region [53, 54], focusing LGBs introduces extra terms in Ω_r [76], which lack a definite OAM transfer as in Eq. (6) and cannot be

eliminated due to the limited tunability of LGBs, thus preventing the emergence of SOAMC. In contrast, our VB-based scheme enables SOAMC by appropriately tuning VB parameters.

Consider $N = 1000$ ^{87}Rb atoms in an optical dipole trap with trapping frequencies $\omega_x = \omega_y = \omega = 2\pi \times 103.3\text{Hz}$ and $\omega_z = 10\omega$, and transverse trap size $a_0 \approx 1.06\mu\text{m}$. Two characteristic energy scales are relevant [39, 53, 54]: $E_r = \hbar^2/2M\bar{w}^2$, characterizing the energy transferred during the Raman process, and $E_L = \Delta l^2/2MR^2$, characterizing the rotational energy with OAM Δl , where \bar{w} is the spot size of tightly focused VB, and R is the atom cloud radius [53]. For the setup in Fig. 2 (c), with $\Delta l = 5$ and $R = 3\mu\text{m}$, we find $E_L \approx h \times 161.35\text{Hz}$. The tightly focused VBs form a doughnut-shaped spot with peak intensity at radius $r_M \approx 2.34a_0 \approx 2.48\mu\text{m}$. Setting $\bar{w} = r_M$, we obtain $E_r \approx h \times 9.43\text{Hz}$, giving $E_L/E_r \approx 17$. The critical coupling strength is $\Omega_0^c \approx 0.82\hbar\omega \approx h \times 84.71\text{Hz}$ at $\delta = 0$, which creates a significantly expanded angular stripe phase region, making it readily achievable in experiments. Thus, compared to LGB-induced SOAMC, our VB-based scheme provides a *three-orders-of-magnitude* enhancement, enabling feasible experimental observation.

Summary.—We proposed a novel scheme using VBs to couple the internal states of ultracold atoms, generating synthetic gauge fields. The ground-state phase diagrams reveal a significantly enhanced angular stripe phase compared to conventional LGB-induced SOAMC, making it experimentally accessible. This approach opens new opportunities for exploring supersolids with azimuthal modulation [80, 81]. Additionally, we presented a mechanism to create topologically nontrivial giant skyrmions without rotation, enabling precise control of topology via optical methods, which could advance the study of skyrmion physics [72, 82, 83] in ultracold atomic systems. These findings highlight the exceptional tunability of VBs, establishing them as powerful tools for quantum control and exploring exotic quantum phenomena.

Acknowledgments.—We acknowledge helpful discussions with Shizhong Zhang, Jiansong Pan, Shanshan Ding, Tianyou Gao, and Lingran Kong. S.Z. acknowledges support from the Youth Innovation Promotion Association, Chinese Academy of Sciences (2023399). X.L. acknowledges support from the National Natural Science Foundation of China (U24A6010, 52488301).

* These authors contributed equally to this work.

† lwg@ioe.ac.cn

- [1] I. Bloch, J. Dalibard, and S. Nascimbene, *Nature Physics* **8**, 267 (2012).
- [2] C. Gross and I. Bloch, *Science* **357**, 995 (2017).
- [3] I. M. Georgescu, S. Ashhab, and F. Nori, *Rev. Mod. Phys.* **86**, 153 (2014).
- [4] M. Saffman, T. G. Walker, and K. Mølmer, *Rev. Mod. Phys.* **82**, 2313 (2010).
- [5] L. Henriët, L. Beguin, A. Signoles, T. Lahaye, A. Browaeys, G.-O. Reymond, and C. Jurczak, *Quantum* **4**, 327 (2020).
- [6] L. Pezzè, A. Smerzi, M. K. Oberthaler, R. Schmied, and P. Treutlein, *Rev. Mod. Phys.* **90**, 035005 (2018).
- [7] I. Bloch, J. Dalibard, and W. Zwerger, *Rev. Mod. Phys.* **80**, 885 (2008).
- [8] Y.-J. Lin, R. L. Compton, K. Jiménez-García, J. V. Porto, and I. B. Spielman, *Nature* **462**, 628 (2009).
- [9] Y.-J. Lin, R. L. Compton, K. Jimenez-Garcia, W. D. Phillips, J. V. Porto, and I. B. Spielman, *Nature Physics* **7**, 531 (2011).
- [10] Y.-J. Lin, K. Jiménez-García, and I. B. Spielman, *Nature* **471**, 83 (2011).
- [11] N. Goldman, G. Juzeliūnas, P. Öhberg, and I. B. Spielman, *Rep. Prog. Phys.* **77**, 126401 (2014).
- [12] H. Zhai, *Reports on Progress in Physics* **78**, 026001 (2015).
- [13] P. Wang, Z.-Q. Yu, Z. Fu, J. Miao, L. Huang, S. Chai, H. Zhai, and J. Zhang, *Phys. Rev. Lett.* **109**, 095301 (2012).
- [14] L. W. Cheuk, A. T. Sommer, Z. Hadzibabic, T. Yefsah, W. S. Bakr, and M. W. Zwierlein, *Phys. Rev. Lett.* **109**, 095302 (2012).
- [15] V. Galitski and I. B. Spielman, *Nature* **494**, 49 (2013).
- [16] L. Huang, Z. Meng, P. Wang, P. Peng, S.-L. Zhang, L. Chen, D. Li, Q. Zhou, and J. Zhang, *Nature Physics* **12**, 540 (2016).
- [17] Z. Wu, L. Zhang, W. Sun, X.-T. Xu, B.-Z. Wang, S.-C. Ji, Y. Deng, S. Chen, X.-J. Liu, and J.-W. Pan, *Science* **354**, 83 (2016).
- [18] Z.-Y. Wang, X.-C. Cheng, B.-Z. Wang, J.-Y. Zhang, Y.-H. Lu, C.-R. Yi, S. Niu, Y. Deng, X.-J. Liu, S. Chen, et al., *Science* **372**, 271 (2021).
- [19] N. Nagaosa, J. Sinova, S. Onoda, A. H. MacDonald, and N. P. Ong, *Reviews of modern physics* **82**, 1539 (2010).
- [20] X.-L. Qi and S.-C. Zhang, *Reviews of modern physics* **83**, 1057 (2011).
- [21] N. P. Armitage, E. J. Mele, and A. Vishwanath, *Rev. Mod. Phys.* **90**, 015001 (2018).
- [22] G. Bihlmayer, P. Noël, D. V. Vyalikh, E. V. Chulkov, and A. Manchon, *Nat. Rev. Phys.* **4**, 642 (2022).
- [23] R. M. Kroeze, Y. Guo, and B. L. Lev, *Phys. Rev. Lett.* **123**, 160404 (2019).
- [24] J. Cabedo and A. Celi, *Phys. Rev. Res.* **3**, 043215 (2021).
- [25] A. Putra, F. Salces-Cárcoba, Y. Yue, S. Sugawa, and I. B. Spielman, *Phys. Rev. Lett.* **124**, 053605 (2020).
- [26] K. T. Geier, G. I. Martone, P. Hauke, and S. Stringari, *Phys. Rev. Lett.* **127**, 115301 (2021).
- [27] C.-H. Li, C. Qu, R. J. Niffenegger, S.-J. Wang, M. He, D. B. Blasing, A. J. Olson, C. H. Greene, Y. Lyanda-Geller, Q. Zhou, et al., *Nature Communications* **10**, 375 (2019).
- [28] H. Wang, L. Wen, H. Yang, C. Shi, and J. Li, *Journal of Physics B: Atomic, Molecular and Optical Physics* **50**, 155301 (2017).
- [29] S. Li, H. Wang, F. Li, X. Cui, and B. Liu, *Physical Review A* **102**, 033328 (2020).
- [30] Q. Liang, Z. Dong, J.-S. Pan, H. Wang, H. Li, Z. Yang, W. Yi, and B. Yan, *Nature Physics* pp. 1–6 (2024).
- [31] A. Mukhopadhyay, X.-W. Luo, C. Schimelfenig, M. Ome, S. Mossman, C. Zhang, and P. Engels, *Physical Review*

- Letters **132**, 233403 (2024).
- [32] M.-C. Liang, Y.-D. Wei, L. Zhang, X.-J. Wang, H. Zhang, W.-W. Wang, W. Qi, X.-J. Liu, and X. Zhang, *Physical Review Research* **5**, L012006 (2023).
- [33] W. Sun, B.-Z. Wang, X.-T. Xu, C.-R. Yi, L. Zhang, Z. Wu, Y. Deng, X.-J. Liu, S. Chen, and J.-W. Pan, *Physical review letters* **121**, 150401 (2018).
- [34] Y. Wang, L. Zhang, S. Niu, D. Yu, and X.-J. Liu, *Phys. Rev. Lett.* **125**, 073204 (2020).
- [35] Z. Zheng, Z. Lin, D.-W. Zhang, S.-L. Zhu, and Z. Wang, *Physical Review Research* **1**, 033102 (2019).
- [36] P. He, M. A. Perlin, S. R. Muleady, R. J. Lewis-Swan, R. B. Hutson, J. Ye, and A. M. Rey, *Physical Review Research* **1**, 033075 (2019).
- [37] M. DeMarco and H. Pu, *Physical Review A* **91**, 033630 (2015).
- [38] K. Sun, C. Qu, and C. Zhang, *Physical Review A* **91**, 063627 (2015).
- [39] C. Qu, K. Sun, and C. Zhang, *Physical Review A* **91**, 053630 (2015).
- [40] Y.-X. Hu, C. Miniatura, and B. Gremaud, *Physical Review A* **92**, 033615 (2015).
- [41] L. Chen, H. Pu, and Y. Zhang, *Physical Review A* **93**, 013629 (2016).
- [42] L. Chen, Y. Zhang, and H. Pu, *Physical Review Letters* **125**, 195303 (2020).
- [43] S.-G. Peng, K. Jiang, X.-L. Chen, K.-J. Chen, P. Zou, and L. He, *AAPPS Bulletin* **32**, 36 (2022).
- [44] E. B. Ng and C. R. Ooi, *Results in Physics* **52**, 106870 (2023).
- [45] K.-J. Chen, F. Wu, S.-G. Peng, W. Yi, and L. He, *Physical Review Letters* **125**, 260407 (2020).
- [46] K.-J. Chen, F. Wu, L. He, and W. Yi, *Physical Review Research* **4**, 033023 (2022).
- [47] X.-L. Chen, S.-G. Peng, P. Zou, X.-J. Liu, and H. Hu, *Physical Review Research* **2**, 033152 (2020).
- [48] K.-J. Chen, F. Wu, J. Hu, and L. He, *Physical Review A* **102**, 013316 (2020).
- [49] Y. Duan, Y. Bidasyuk, and A. Surzhykov, *Physical Review A* **102**, 063328 (2020).
- [50] N. Chiu, Y. Kawaguchi, S. Yip, and Y. Lin, *New Journal of Physics* **22**, 093017 (2020).
- [51] Y. Bidasyuk, K. Kovtunenkov, and O. Prikhodko, *Physical Review A* **105**, 023320 (2022).
- [52] L.-L. Wang, A.-C. Ji, Q. Sun, and J. Li, *Physical Review Letters* **126**, 193401 (2021).
- [53] D. Zhang, T. Gao, P. Zou, L. Kong, R. Li, X. Shen, X.-L. Chen, S.-G. Peng, M. Zhan, H. Pu, et al., *Physical Review Letters* **122**, 110402 (2019).
- [54] H.-R. Chen, K.-Y. Lin, P.-K. Chen, N.-C. Chiu, J.-B. Wang, C.-A. Chen, P. Huang, S.-K. Yip, Y. Kawaguchi, and Y.-J. Lin, *Physical Review Letters* **121**, 113204 (2018).
- [55] A. Forbes, M. de Oliveira, and M. R. Dennis, *Nat. Photonics* **15**, 253 (2021).
- [56] C. Rosales-Guzmán, B. Ndagano, and A. Forbes, *Journal of Optics* **20**, 123001 (2018).
- [57] Y. Shen, X. Wang, Z. Xie, C. Min, X. Fu, Q. Liu, M. Gong, and X. Yuan, *Light Sci Appl* **8**, 90 (2019).
- [58] Q. Zhan, *Advances in Optics and Photonics* **1**, 1 (2009).
- [59] F. Zhang, H. Yu, J. Fang, M. Zhang, S. Chen, J. Wang, A. He, and J. Chen, *Optics Express* **24**, 6656 (2016).
- [60] Y. Guo, S. Zhang, M. Pu, Q. He, J. Jin, M. Xu, Y. Zhang, P. Gao, and X. Luo, *Light: Science & Applications* **10**, 63 (2021).
- [61] X. Luo, M. Pu, F. Zhang, M. Xu, Y. Guo, X. Li, and X. Ma, *J. Appl. Phys.* **131**, 181101 (2022).
- [62] J. Feng, H. Shi, J. Yi, A. Zhang, S. N. Burokur, J. Chen, X. Chen, and Z. Xu, *Physical Review Applied* **19**, 044075 (2023).
- [63] F. Alsolamy and A. Grbic, *Physical Review Applied* **22**, 014001 (2024).
- [64] J. Wang, F. Castellucci, and S. Franke-Arnold, *AVS Quantum Science* **2** (2020).
- [65] F. Castellucci, T. W. Clark, A. Selyem, J. Wang, and S. Franke-Arnold, *Physical Review Letters* **127**, 233202 (2021).
- [66] N. Radwell, T. W. Clark, B. Piccirillo, S. M. Barnett, and S. Franke-Arnold, *Physical Review Letters* **114**, 123603 (2015).
- [67] S.-J. Yang, Q.-S. Wu, S.-N. Zhang, and S. Feng, *Physical Review A—Atomic, Molecular, and Optical Physics* **77**, 033621 (2008).
- [68] P. Mason and A. Aftalion, *Physical Review A—Atomic, Molecular, and Optical Physics* **84**, 033611 (2011).
- [69] J. Jin, S. Zhang, W. Han, and Z. Wei, *Journal of Physics B: Atomic, Molecular and Optical Physics* **46**, 075302 (2013).
- [70] M. Ezawa, *Phys. Rev. Lett.* **105**, 197202 (2010).
- [71] B. Dong, Q. Sun, W.-M. Liu, A.-C. Ji, X.-F. Zhang, and S.-G. Zhang, *Phys. Rev. A* **96**, 013619 (2017).
- [72] G. Zhang, Q. Luo, X. Wen, H. Wu, L. Yang, W. Jin, L. Li, J. Zhang, W. Zhang, H. Shu, et al., *Chinese Physics Letters* **40**, 117501 (2023).
- [73] G. Milione, H. I. Sztul, D. A. Nolan, and R. R. Alfano, *Phys. Rev. Lett.* **107**, 053601 (2011).
- [74] Z. Chen, L. Hua, and J. Pu, *Progress in Optics* **57**, 219 (2012).
- [75] P. Yu, Y. Liu, Z. Wang, Y. Li, and L. Gong, *Annalen Der Physik* **532**, 2000110 (2020).
- [76] See Supplementary Material for the explicit expressions of the tightly focused VBs' electric fields, the detailed energy level configuration, the derivation of Hamiltonians, the VB-induced potentials for varying VB parameters, and the analysis of spin textures, which includes Refs. [84–87].
- [77] M. L. Chiofalo, S. Succi, and M. Tosi, *Physical Review E* **62**, 7438 (2000).
- [78] W. Bao and Q. Du, *SIAM Journal on Scientific Computing* **25**, 1674 (2004).
- [79] N. Manton and P. Sutcliffe, *Topological solitons* (Cambridge University Press, Cambridge, England, 2004).
- [80] L. Tanzi, J. Maloberti, G. Biagioni, A. Fioretti, C. Gabbanini, and G. Modugno, *Science* **371**, 1162 (2021).
- [81] J.-R. Li, J. Lee, W. Huang, S. Burchesky, B. Shteynas, F. Ç. Top, A. O. Jamison, and W. Ketterle, *Nature* **543**, 91 (2017).
- [82] A. Fert, V. Cros, and J. Sampaio, *Nature nanotechnology* **8**, 152 (2013).
- [83] C. Psaroudaki and C. Panagopoulos, *Physical Review Letters* **127**, 067201 (2021).
- [84] B. Richards and E. Wolf, *Proceedings of the Royal Society of London. Series A. Mathematical and Physical Sciences* **253**, 358 (1959).
- [85] F. Le Kien, P. Schneeweiss, and A. Rauschenbeutel, *Eur. Phys. J. D* **67**, 1 (2013).
- [86] C. J. Pethick and H. Smith, *Bose-Einstein condensation in dilute gases* (Cambridge University Press, Cambridge,

England, 2018), 2nd ed.

[87] X. Su, W. Dai, T. Li, J. Wang, and L. Wen, *Chaos, Solitons & Fractals* **184**, 114979 (2024).

Supplemental Material: Synthetic Gauge Field for Ultracold Atoms Induced by Vector Beams

Huan Wang,^{1,2,3,*} Shangguo Zhu,^{1,2,3,4,*} Yun Long,^{1,2,3,4} Mingbo Pu,^{1,2,3,4} and Xiangang Luo^{1,2,4,†}

¹National Key Laboratory of Optical Field Manipulation Science and Technology,
Chinese Academy of Sciences, Chengdu 610209, China

²State Key Laboratory of Optical Technologies on Nano-Fabrication and Micro-Engineering,
Institute of Optics and Electronics, Chinese Academy of Sciences, Chengdu 610209, China

³Research Center on Vector Optical Fields, Institute of Optics and Electronics,
Chinese Academy of Sciences, Chengdu 610209, China

⁴College of Materials Science and Opto-Electronic Technology,
University of Chinese Academy of Sciences, Beijing 100049, China

In this Supplemental Material (SM), we provide further details on the explicit expressions of electric fields of the tightly focused vector beams (VBs), the detailed energy level configuration, the derivation of the Hamiltonians for the single-particle and weakly interacting cases, the VB-induced potentials for varying VB parameters, and the analysis of spin textures.

S-1. ELECTRIC FIELDS OF TIGHTLY FOCUSED VECTOR BEAMS

We introduce the electric fields of tightly focused VBs after passing through a high-numerical-aperture (NA) lens, as shown in Fig. 1 of the main text. The electric field at the focal plane are determined using Richards-Wolf vectorial diffraction integral [S1–S3] in the cylindrical coordinates (ρ, φ, z) , given by:

$$E_x = i^{a+1} \cos(\alpha/2) e^{-i\beta/2} \left[e^{ia\varphi} \mathcal{I}_a + e^{i(a+2)\varphi} \mathcal{I}_{a+2}'' \right] + i^{b+1} \sin(\alpha/2) e^{i\beta/2} \left[e^{ib\varphi} \mathcal{I}_b + e^{i(b-2)\varphi} \mathcal{I}_{b-2}'' \right], \quad (\text{S1})$$

$$E_y = i^{a+2} \cos(\alpha/2) e^{-i\beta/2} \left[e^{ia\varphi} \mathcal{I}_a - e^{i(a+2)\varphi} \mathcal{I}_{a+2}'' \right] + i^b \sin(\alpha/2) e^{i\beta/2} \left[e^{ib\varphi} \mathcal{I}_b - e^{i(b-2)\varphi} \mathcal{I}_{b-2}'' \right], \quad (\text{S2})$$

$$E_z = -i^{a+2} \cos(\alpha/2) e^{-i\beta/2} e^{i(a+1)\varphi} \mathcal{I}_{a+1}' - i^b \sin(\alpha/2) e^{i\beta/2} e^{i(b-1)\varphi} \mathcal{I}_{b-1}', \quad (\text{S3})$$

where $a \equiv l - m$, and $b \equiv l + m$. α and β are spherical coordinates of high-order Poincaré sphere as shown in Fig. 1 (b). \mathcal{I}_n , \mathcal{I}_n' , and \mathcal{I}_n'' depend on spatial coordinates ρ and z , expressed as

$$\mathcal{I}_n = -kF \int_0^{\theta_{\max}} d\theta \bar{A}_l(\theta) \sin \theta \cos^{1/2}(\theta) (1 + \cos \theta) e^{ikz \cos \theta} J_n(k\rho \sin \theta), \quad (\text{S4})$$

$$\mathcal{I}_n' = -2kF \int_0^{\theta_{\max}} d\theta \bar{A}_l(\theta) \sin^2 \theta \cos^{1/2}(\theta) e^{ikz \cos \theta} J_n(k\rho \sin \theta), \quad (\text{S5})$$

$$\mathcal{I}_n'' = -kF \int_0^{\theta_{\max}} d\theta \bar{A}_l(\theta) \sin \theta \cos^{1/2}(\theta) (1 - \cos \theta) e^{ikz \cos \theta} J_n(k\rho \sin \theta), \quad (\text{S6})$$

where $k = 2\pi/\lambda$ is the wave number, λ is the wavelength, and $J_n(x)$ denotes the n -th order Bessel function of the first kind. The angle θ is defined for the point $(\rho, \varphi, z = -F)$ on the plane where the high-NA lens (with focal length F) is located, such that $\sin \theta = \rho/F$ and $0 \leq \theta \leq \theta_{\max}$ with $\sin \theta_{\max} = \text{NA}$. The amplitude profile $\bar{A}_l(\theta)$ is given by

$$\bar{A}_l(\theta) = \sqrt{I} \left[\frac{\sqrt{2}\zeta \sin(\theta)}{\sin(\theta_{\max})} \right]^{|l|} \exp \left[-\zeta^2 \left(\frac{\sin(\theta)}{\sin(\theta_{\max})} \right)^2 \right], \quad (\text{S7})$$

where $\zeta = F \sin(\theta_{\max})/w$. In this work, we use a high-NA lens with $\text{NA} = 0.8$, $F = 1.95\text{mm}$, and set $\zeta = 8$ (or $w = 0.195\text{mm}$).

* These authors contributed equally to this work.

† lxg@ioe.ac.cn

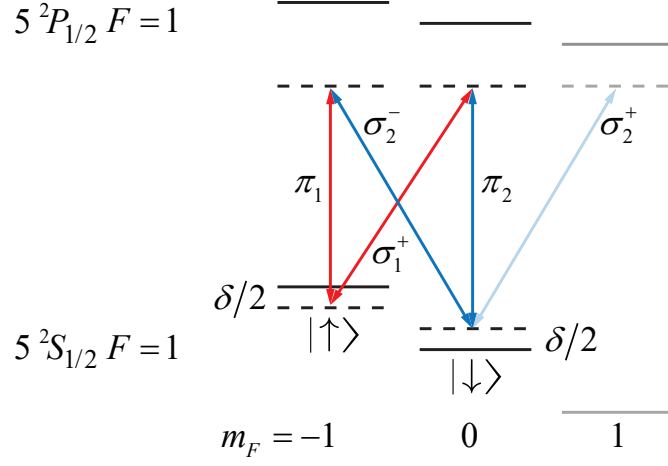


FIG. S1. Double- Λ -type energy level configuration. Optical transitions allowed by the selection rules involve the σ_1^+ and π_2 components or the π_1 and σ_2^- components of the tightly focused VBs with optical frequencies ω_1 (red) and ω_2 (blue).

S-2. SINGLE-PARTICLE HAMILTONIAN

We consider $N = 1000$ ^{87}Rb atoms trapped in an optical dipole trap with trapping frequencies $\omega_x = \omega_y = \omega = 2\pi \times 103.3\text{Hz}$ and $\omega_z = 10\omega$, and transverse trap size $a_0 \approx 1.06\mu\text{m}$. The system includes Zeeman sublevels $|\downarrow\rangle \equiv |5^2S_{1/2}, F=1, m_F=0\rangle$ and $|\uparrow\rangle \equiv |5^2S_{1/2}, F=1, m_F=-1\rangle$, and the excited states $|5^2P_{1/2}, F=1, m_F=0\rangle$ and $|5^2P_{1/2}, F=1, m_F=-1\rangle$, forming a double- Λ -type energy level configuration as shown in Fig. S1 and Fig. 1 (c) of the main text. The states $|\uparrow\rangle$ and $|\downarrow\rangle$ are coupled via two-photon Raman processes, obeying the selection rules for the σ_1^+ and π_2 components, or the π_1 and σ_2^- components of the tightly focused VBs.

The single-particle Hamiltonian is given by

$$H_0 = -\frac{\hbar^2 \nabla^2}{2M} + \frac{1}{2}M\omega^2 \rho^2 + \frac{1}{2}M\omega_z^2 z^2 + h_{\text{eff}}, \quad (\text{S8})$$

where h_{eff} is the effective Hamiltonian for atoms in the ground-state manifold during the Raman process, expressed as [S4–S7]

$$h_{\text{eff}} = u_s |\tilde{\mathbf{E}}|^2 + \frac{\mu_B g_F}{\hbar} (\mathbf{B} + \mathbf{B}_{\text{eff}}) \cdot \mathbf{F}. \quad (\text{S9})$$

The first term represents the scalar light shift, while the second term contains the effective magnetic field

$$\mathbf{B}_{\text{eff}} = \frac{i u_v (\tilde{\mathbf{E}}^* \times \tilde{\mathbf{E}})}{\mu_B g_J}, \quad (\text{S10})$$

which is generated by the vector light shift. u_s and u_v are the scalar and vector polarizabilities, respectively [S4–S7]. The vector light shift induces coupling between different spin states. In our scheme, the total electric field experienced by the atoms is given by

$$\tilde{\mathbf{E}} = \mathbf{E}_1 e^{i\omega_1 t} + \mathbf{E}_2 e^{i\omega_2 t}, \quad (\text{S11})$$

where $\mathbf{E}_1 = (E_{x1}, E_{y1}, E_{z1})$ and $\mathbf{E}_2 = (E_{x2}, E_{y2}, E_{z2})$. We find the potential induced by scalar light shift

$$V_S(\mathbf{r}) = u_s (\mathbf{E}_1^* \cdot \mathbf{E}_1 + \mathbf{E}_2^* \cdot \mathbf{E}_2), \quad (\text{S12})$$

and the effective potential $\mathbf{B}_{\text{eff}} = (B_x, B_y, B_z)$ has components

$$\begin{aligned} B_x &= \frac{i u_v}{\mu_B g_J} \left[(E_{y1}^* E_{z2} - E_{z1}^* E_{y2}) e^{-i(\omega_1 - \omega_2)t} + (E_{y2}^* E_{z1} - E_{z2}^* E_{y1}) e^{i(\omega_1 - \omega_2)t} \right], \\ B_y &= \frac{i u_v}{\mu_B g_J} \left[(E_{z1}^* E_{x2} - E_{x1}^* E_{z2}) e^{-i(\omega_1 - \omega_2)t} + (E_{z2}^* E_{x1} - E_{x2}^* E_{z1}) e^{i(\omega_1 - \omega_2)t} \right], \\ B_z &= \frac{i u_v}{\mu_B g_J} (E_{x1}^* E_{y1} - E_{y1}^* E_{x1} + E_{x2}^* E_{y2} - E_{y2}^* E_{x2}). \end{aligned} \quad (\text{S13})$$

Here we have neglected the terms corresponding to the forbidden optical transitions.

The effective Hamiltonian is reduced to [S5–S7]

$$h_{\text{eff}} = V_S(\mathbf{r}) + \frac{\mu_B g_F}{2} (B_z \sigma_z + B_x \sigma_x + B_y \sigma_y). \quad (\text{S14})$$

After performing the rotating wave approximation and a unitary transformation with $U = e^{i(\omega_1 - \omega_2)t\hat{\sigma}_z/2}$, the single-particle Hamiltonian becomes

$$H_0 = -\frac{\hbar^2 \nabla^2}{2M} + \frac{1}{2} M \omega^2 \rho^2 + \frac{1}{2} M \omega_z^2 z^2 + V_S(\mathbf{r}) + \frac{\delta}{2} \sigma_z + \begin{pmatrix} \Omega_z(\mathbf{r}) & \Omega_r(\mathbf{r}) \\ \Omega_r^*(\mathbf{r}) & -\Omega_z(\mathbf{r}) \end{pmatrix}, \quad (\text{S15})$$

where

$$V_S(\mathbf{r}) = \Omega_s (\bar{\mathbf{E}}_1^* \cdot \bar{\mathbf{E}}_1 + \bar{\mathbf{E}}_2^* \cdot \bar{\mathbf{E}}_2), \quad (\text{S16})$$

$$\Omega_z(\mathbf{r}) = \Omega_0 i (\bar{E}_{x1}^* \bar{E}_{y1} - \bar{E}_{y1}^* \bar{E}_{x1} + \bar{E}_{x2}^* \bar{E}_{y2} - \bar{E}_{y2}^* \bar{E}_{x2}), \quad (\text{S17})$$

$$\Omega_r(\mathbf{r}) = \Omega_0 [(\bar{E}_{z2}^* \bar{E}_{x1} - \bar{E}_{x2}^* \bar{E}_{z1}) + i(\bar{E}_{y2}^* \bar{E}_{z1} - \bar{E}_{z2}^* \bar{E}_{y1})], \quad (\text{S18})$$

and the coupling strengths are

$$\Omega_s = u_s (I_1 + I_2), \quad (\text{S19})$$

$$\Omega_0 = \frac{u_v g_F \sqrt{I_1 I_2}}{2g_J}. \quad (\text{S20})$$

Here I_1 and I_2 are the light intensities of the two VBs, and $\bar{\mathbf{E}}_j = \mathbf{E}_j / \sqrt{I_j} = (\bar{E}_{xj}, \bar{E}_{yj}, \bar{E}_{zj})$ is the normalized electric fields. When interatomic interactions are weak, the motion of atoms can be approximated as a two-dimensional problem [S8–S11]. We focus on the physics near the focal plane at $z = 0$, and the potentials approximately reduce to $V_S(\mathbf{r}) = V_S(\boldsymbol{\rho})$, $\Omega_z(\mathbf{r}) = \Omega_z(\boldsymbol{\rho})$, and $\Omega_r(\mathbf{r}) = \Omega_r(\boldsymbol{\rho})$.

In the main text, for the angular stripe phase in Fig. 2, we adopt a wavelength of $\lambda = 797\text{nm}$. Ω_s is set to be finite and negative, inducing annular confinement via $V_S(\boldsymbol{\rho})$. We find the ratio $\Omega_0/\Omega_s = -\frac{u_v \sqrt{I_1 I_2}}{8u_s (I_1 + I_2)}$, and $u_v/u_s \approx 1.42$ for $\lambda = 797\text{nm}$ [S4]. Given Ω_s , Ω_0 can be tuned by adjusting the intensities I_1 and I_2 of the VBs, making the angular stripe phase experimentally accessible. In Fig. 3 of the main text, we adopt the tune-out wavelength $\lambda = 790\text{nm}$, where the scalar polarizability vanishes, so $\Omega_s \approx 0$. Here the coupling strength Ω_0 is also tunable by adjusting two VBs' light intensities.

S-3. WEAKLY INTERACTING CONDENSATE

We now consider the weakly interacting case. The Gross-Pitaevskii (GP) equation is given by

$$i\hbar \frac{\partial}{\partial t} \Psi^{3\text{D}} = (H_0 + V_1) \Psi^{3\text{D}}, \quad (\text{S21})$$

where V_1 represents the mean-field interaction:

$$V_1(\mathbf{r}) = \begin{pmatrix} g_{\uparrow\uparrow} |\psi_{\uparrow}^{3\text{D}}(\mathbf{r})|^2 + g_{\uparrow\downarrow} |\psi_{\downarrow}^{3\text{D}}(\mathbf{r})|^2 & 0 \\ 0 & g_{\uparrow\downarrow} |\psi_{\uparrow}^{3\text{D}}(\mathbf{r})|^2 + g_{\downarrow\downarrow} |\psi_{\downarrow}^{3\text{D}}(\mathbf{r})|^2 \end{pmatrix}. \quad (\text{S22})$$

Here $g_{\sigma\sigma'} = 4\pi\hbar^2 N a_{\sigma\sigma'}^s / M$ is the nonlinear interaction strength, $a_{\sigma\sigma'}^s$ is the s-wave scattering length between two spins $\sigma = \uparrow, \downarrow$, and N is total number of atoms.

In our scheme, we consider a pancake-shaped Bose-Einstein condensate (BEC) with the trapping frequency $\omega_z \gg \omega$. The wave function is approximated as

$$\Psi^{3\text{D}} = \begin{pmatrix} \psi_{\uparrow}(\boldsymbol{\rho}) \\ \psi_{\downarrow}(\boldsymbol{\rho}) \end{pmatrix} \psi^{1\text{D}}(z). \quad (\text{S23})$$

Inserting Eqs. (S15), (S22) and (S23) into the GP equation, and integrating both sides with respect to z [S9], we obtain

$$i\hbar \frac{\partial \psi_{\uparrow}}{\partial t} = \left[-\frac{\hbar^2 \nabla_{\rho}^2}{2M} + \frac{1}{2} M \omega^2 \rho^2 + V_S(\boldsymbol{\rho}) + \frac{\delta}{2} + \Omega_z(\boldsymbol{\rho}) + \eta (g_{\uparrow\uparrow} |\psi_{\uparrow}|^2 + g_{\uparrow\downarrow} |\psi_{\downarrow}|^2) \right] \psi_{\uparrow} + C \psi_{\uparrow} + \Omega_r(\boldsymbol{\rho}) \psi_{\downarrow}, \quad (\text{S24})$$

$$i\hbar \frac{\partial \psi_{\downarrow}}{\partial t} = \left[-\frac{\hbar^2 \nabla_{\rho}^2}{2M} + \frac{1}{2} M \omega^2 \rho^2 + V_S(\boldsymbol{\rho}) - \frac{\delta}{2} - \Omega_z(\boldsymbol{\rho}) + \eta (g_{\uparrow\downarrow} |\psi_{\uparrow}|^2 + g_{\downarrow\downarrow} |\psi_{\downarrow}|^2) \right] \psi_{\downarrow} + C \psi_{\downarrow} + \Omega_r^*(\boldsymbol{\rho}) \psi_{\uparrow}. \quad (\text{S25})$$

Here the constant C and the dimensional reduction factor η are defined as

$$\eta = \frac{\int_z |\psi^{1D}(z)|^4 dz}{\int_z |\psi^{1D}(z)|^2 dz}, \quad C = \frac{\hbar^2 \int_z \left| \frac{d\psi^{1D}(z)}{dz} \right|^2 dz}{2M \int_z |\psi^{1D}(z)|^2 dz} + \frac{1}{2} M \omega_z^2 \frac{\int_z z^2 |\psi^{1D}(z)|^2 dz}{\int_z |\psi^{1D}(z)|^2 dz}. \quad (\text{S26})$$

Substituting $\psi_\sigma = \exp(-iCt/\hbar)\tilde{\psi}_\sigma$, and replacing $\tilde{\psi}_\sigma \rightarrow \psi_\sigma$, we obtain the reduced two-dimensional GP equation

$$i\hbar \frac{\partial \psi_\uparrow}{\partial t} = \left[-\frac{\hbar^2 \nabla_\rho^2}{2M} + \frac{1}{2} M \omega^2 \rho^2 + V_S(\boldsymbol{\rho}) + \frac{\delta}{2} + \Omega_z(\boldsymbol{\rho}) + \eta \left(g_{\uparrow\uparrow} |\psi_\uparrow|^2 + g_{\uparrow\downarrow} |\psi_\downarrow|^2 \right) \right] \psi_\uparrow + \Omega_r(\boldsymbol{\rho}) \psi_\downarrow, \quad (\text{S27})$$

$$i\hbar \frac{\partial \psi_\downarrow}{\partial t} = \left[-\frac{\hbar^2 \nabla_\rho^2}{2M} + \frac{1}{2} M \omega^2 \rho^2 + V_S(\boldsymbol{\rho}) - \frac{\delta}{2} - \Omega_z(\boldsymbol{\rho}) + \eta \left(g_{\downarrow\downarrow} |\psi_\downarrow|^2 + g_{\downarrow\uparrow} |\psi_\uparrow|^2 \right) \right] \psi_\downarrow + \Omega_r^*(\boldsymbol{\rho}) \psi_\uparrow. \quad (\text{S28})$$

Moreover, the 1D wave function $\psi^{1D}(z)$ is given by form [S12]

$$\psi^{1D}(z) = \frac{e^{-z^2/2a_{0z}^2}}{\pi^{1/4} a_{0z}^{1/2}}, \quad (\text{S29})$$

where $a_{0z} \equiv \sqrt{\hbar/M\omega_z}$ is the trap size along the z -axis. Therefore, the dimensional reduction factor is $\eta = 1/(\sqrt{2\pi}a_{0z})$.

S-4. THE FORMS OF Ω_r AND Ω_z FOR VARYING VB PARAMETERS

To analytically demonstrate the forms of $\Omega_r(\boldsymbol{\rho})$ and $\Omega_z(\boldsymbol{\rho})$, we substitute the electric fields from Eqs. (S1)-(S3) into the last term of Eq. (S15). For simplicity, assuming both VBs have the same orientation angle $\beta_1 = \beta_2 = 0$, we obtain

$$\Omega_r(\boldsymbol{\rho}) = f_r^1(\rho) \Theta_r^1(\alpha_1, \alpha_2) e^{i\tilde{l}_1 \varphi} + f_r^2(\rho) \Theta_r^2(\alpha_1, \alpha_2) e^{i\tilde{l}_2 \varphi} + f_r^3(\rho) \Theta_r^3(\alpha_1, \alpha_2) e^{i\tilde{l}_3 \varphi} + f_r^4(\rho) \Theta_r^4(\alpha_1, \alpha_2) e^{i\tilde{l}_4 \varphi}, \quad (\text{S30})$$

$$\begin{aligned} \Omega_z(\boldsymbol{\rho}) &= f_z^1(\rho) \Theta_z^1(\alpha_1) + f_z^2(\rho) \Theta_z^2(\alpha_2) + f_z^3(\rho) \Theta_z^3(\alpha_1) + f_z^4(\rho) \Theta_z^4(\alpha_2) \\ &+ f_z^5(\rho) \Theta_z^5(\alpha_1) e^{i\tilde{l}_5 \varphi} + f_z^6(\rho) \Theta_z^6(\alpha_1) e^{-i\tilde{l}_5 \varphi} + f_z^7(\rho) \Theta_z^7(\alpha_2) e^{i\tilde{l}_6 \varphi} + f_z^8(\rho) \Theta_z^8(\alpha_2) e^{-i\tilde{l}_6 \varphi}, \end{aligned} \quad (\text{S31})$$

with

$$\begin{aligned} f_r^1(\rho) &= 2i^{a_1+1} (-i)^{a_2} (\mathcal{I}_{a_1} \mathcal{I}'_{a_2+1} + \mathcal{I}'_{a_1+1} \mathcal{I}''_{a_2+2}), & \Theta_r^1(\alpha_1, \alpha_2) &= \cos(\alpha_1/2) \cos(\alpha_2/2), \\ f_r^2(\rho) &= 2i^{a_1+1} (-i)^{b_2} (\mathcal{I}'_{a_1+1} \mathcal{I}_{b_2} - \mathcal{I}_{a_1} \mathcal{I}'_{b_2-1}), & \Theta_r^2(\alpha_1, \alpha_2) &= \cos(\alpha_1/2) \sin(\alpha_2/2), \\ f_r^3(\rho) &= 2i^{b_1+1} (-i)^{a_2} (\mathcal{I}''_{b_1-2} \mathcal{I}'_{a_2+1} - \mathcal{I}'_{b_1-1} \mathcal{I}''_{a_2+2}), & \Theta_r^3(\alpha_1, \alpha_2) &= \sin(\alpha_1/2) \cos(\alpha_2/2), \\ f_r^4(\rho) &= -2i^{b_1+1} (-i)^{b_2} (\mathcal{I}'_{b_1-1} \mathcal{I}_{b_2} + \mathcal{I}''_{b_1-2} \mathcal{I}'_{b_2-1}), & \Theta_r^4(\alpha_1, \alpha_2) &= \sin(\alpha_1/2) \sin(\alpha_2/2), \\ f_z^1(\rho) &= -2(\mathcal{I}_{a_1}^2 - \mathcal{I}''_{a_1+2}), & \Theta_z^1(\alpha_1) &= \cos^2(\alpha_1/2), \\ f_z^2(\rho) &= -2(\mathcal{I}_{a_2}^2 - \mathcal{I}''_{a_2+2}), & \Theta_z^2(\alpha_2) &= \cos^2(\alpha_2/2), \\ f_z^3(\rho) &= 2(\mathcal{I}_{b_1}^2 - \mathcal{I}''_{b_1-2}), & \Theta_z^3(\alpha_1) &= \sin^2(\alpha_1/2), \\ f_z^4(\rho) &= 2(\mathcal{I}_{b_2}^2 - \mathcal{I}''_{b_2-2}), & \Theta_z^4(\alpha_2) &= \sin^2(\alpha_2/2), \\ f_z^5(\rho) &= (-i)^{b_1} i^{a_1} (\mathcal{I}''_{a_1+2} \mathcal{I}_{b_1} - \mathcal{I}_{a_1} \mathcal{I}''_{b_1-2}), & \Theta_z^5(\alpha_1) &= \sin(\alpha_1), \\ f_z^6(\rho) &= (-i)^{a_1} i^{b_1} (\mathcal{I}''_{a_1+2} \mathcal{I}_{b_1} - \mathcal{I}_{a_1} \mathcal{I}''_{b_1-2}), & \Theta_z^6(\alpha_1) &= \sin(\alpha_1), \\ f_z^7(\rho) &= (-i)^{b_2} i^{a_2} (\mathcal{I}''_{a_2+2} \mathcal{I}_{b_2} - \mathcal{I}_{a_2} \mathcal{I}''_{b_2-2}), & \Theta_z^7(\alpha_2) &= \sin(\alpha_2), \\ f_z^8(\rho) &= (-i)^{a_2} i^{b_2} (\mathcal{I}''_{a_2+2} \mathcal{I}_{b_2} - \mathcal{I}_{a_2} \mathcal{I}''_{b_2-2}), & \Theta_z^8(\alpha_2) &= \sin(\alpha_2). \end{aligned}$$

The f -functions with subscript r only depend on the spatial variable ρ . Here $a_j = l_j - m_j$ and $b_j = l_j + m_j$ with $j = 1, 2$. α_1 and α_2 denote the ellipticity angles on the high-order Poincaré sphere. We define the effective topological charges

TABLE S1. Ω_r and Ω_z for different sets of VB parameters

Scenario	Ω_r/Ω_0	Ω_z/Ω_0	note
1. $\alpha_1 = 0, \alpha_2 = 0$	$f_r^1 e^{i\bar{l}\varphi}$	$f_z^1 + f_z^2$	$\bar{l} = \bar{l}_1$
2. $\alpha_1 = 0, \alpha_2 = \pi$	$f_r^2 e^{i\bar{l}\varphi}$	$f_z^1 + f_z^2$	$\bar{l} = \bar{l}_2$
3. $\alpha_1 = \pi, \alpha_2 = 0$	$f_r^3 e^{i\bar{l}\varphi}$	$f_z^3 + f_z^4$	$\bar{l} = \bar{l}_3$
4. $\alpha_1 = \pi, \alpha_2 = \pi$	$f_r^4 e^{i\bar{l}\varphi}$	$f_z^3 + f_z^4$	$\bar{l} = \bar{l}_4$
5. $\alpha_1 = 0, \alpha_2 = \forall$ <i>Cond</i> : $m_2 = 1$	$[f_r^1 \Theta_r^1 + f_r^2 \Theta_r^2] e^{i\bar{l}\varphi}$	$f_z^1 + f_z^2 \Theta_z^2 + f_z^4 \Theta_z^4$ $+ f_z^7 \Theta_z^7 + f_z^8 \Theta_z^8$	$\bar{l} = \bar{l}_1 = \bar{l}_2$
6. $\alpha_1 = \pi, \alpha_2 = \forall$ <i>Cond</i> : $m_2 = 1$	$[f_r^3 \Theta_r^3 + f_r^4 \Theta_r^4] e^{i\bar{l}\varphi}$	$f_z^3 + f_z^2 \Theta_z^2 + f_z^4 \Theta_z^4$ $+ f_z^7 \Theta_z^7 + f_z^8 \Theta_z^8$	$\bar{l} = \bar{l}_3 = \bar{l}_4$
7. $\alpha_1 = \forall, \alpha_2 = 0$ <i>Cond</i> : $m_1 = 1$	$[f_r^1 \Theta_r^1 + f_r^3 \Theta_r^3] e^{i\bar{l}\varphi}$	$f_z^2 + f_z^1 \Theta_z^1 + f_z^3 \Theta_z^3$ $+ f_z^5 \Theta_z^5 + f_z^6 \Theta_z^6$	$\bar{l} = \bar{l}_1 = \bar{l}_3$
8. $\alpha_1 = \forall, \alpha_2 = \pi$ <i>Cond</i> : $m_1 = 1$	$[f_r^2 \Theta_r^2 + f_r^4 \Theta_r^4] e^{i\bar{l}\varphi}$	$f_z^4 + f_z^1 \Theta_z^1 + f_z^3 \Theta_z^3$ $+ f_z^5 \Theta_z^5 + f_z^6 \Theta_z^6$	$\bar{l} = \bar{l}_2 = \bar{l}_4$
9. $\alpha_1 \neq 0, \pi; \alpha_2 \neq 0, \pi$ <i>Cond</i> : $m_1 = m_2 = 1$ $l_1 = n, l_2 = -n$	$f(\rho) e^{i(2n-1)\varphi}$ ($n \in \forall\mathbb{Z}$)	0	
10. $\alpha_1 \neq 0, \pi; \alpha_2 \neq 0, \pi$ <i>Cond</i> : $m_1 = m_2 = 1$ $l_1 - l_2 = n, l_1 + l_2 \neq 0$	$f(\rho) e^{i(n-1)\varphi}$ ($n \in \forall\mathbb{Z}$)	$f_z(\rho)$	

as:

$$\begin{aligned}
\bar{l}_1 &= l_1 - l_2 - m_1 + m_2 - 1, \\
\bar{l}_2 &= l_1 - l_2 - m_1 - m_2 + 1, \\
\bar{l}_3 &= l_1 - l_2 + m_1 + m_2 - 3, \\
\bar{l}_4 &= l_1 - l_2 + m_1 - m_2 - 1, \\
\bar{l}_5 &= 2 - 2m_1, \\
\bar{l}_6 &= 2 - 2m_2.
\end{aligned} \tag{S32}$$

By varying the VB parameters $(l_j, m_j, \alpha_j, \beta_j)$ with $j = 1, 2$, we can adjust the forms of $\Omega_r(\rho)$ and $\Omega_z(\rho)$, leading to different potentials for the atoms. The specific forms of $\Omega_r(\rho)$ and $\Omega_z(\rho)$ for various VB parameters are presented in Table S1.

Scenarios 1-4. Ω_r simplifies to a single term with a definite effective topological charge \bar{l} , representing the orbital angular momentum (OAM) transfer, while Ω_z reduces to a superposition of two spatially dependent terms.

Scenarios 5-8. If only one of α_1 and α_2 is 0 or π , both Ω_r and Ω_z still exhibit a definite effective topological charge \bar{l} , but include additional spatially dependent terms in ρ .

Scenario 9. For the general cases, with $\alpha_1 \neq 0$ or π and $\alpha_2 \neq 0$ or π , we consider the case $m_1 = m_2 = 1$ and $l_1 = -l_2 = n$, resulting in $\Omega_z = 0$ and $\Omega_r = \Omega_0 f(\rho) e^{i(2n-1)\varphi}$, with $f(\rho) = \sum_{j'=1}^4 f_r^{j'} \Theta_r^{j'}$. Here, Ω_r couples atomic spin and OAM, leading to an OAM transfer $\Delta l = (2n-1)$ for transition $|\uparrow\rangle \rightarrow |\downarrow\rangle$ and $\Delta l = -(2n-1)$ for the reverse. This coupling resembles spin-orbit-angular-momentum coupling (SOAMC) [S9–S11, S13–S18], with the OAM transfer tunable via VB parameters.

Scenario 10. With $\alpha_1 \neq 0$ or π , $\alpha_2 \neq 0$ or π , $m_1 = m_2 = 1$, and $l_1 - l_2 = n$, the effective topological charge becomes $(n-1)$. $\Omega_z = \Omega_0 f_z(\rho)$ introduces a spatially dependent Zeeman shift, where $f_z(\rho) = \sum_{j'=1}^8 f_z^{j'} \Theta_z^{j'}$. Note that this feature is absent in Laguerre-Gaussian-beam (LGB)-induced scheme. Thus, VBs provide additional tunable degrees of freedom for the quantum control of ultracold atoms.

In Fig. S2, we show the polarization and spatial distributions for specific VB parameters. In Fig. S2 (a), for $\alpha = 0$ or

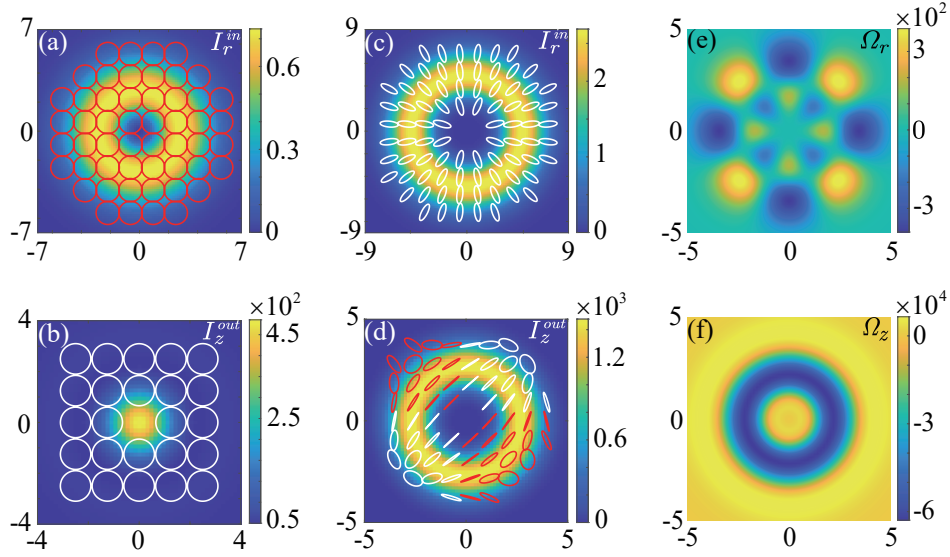


FIG. S2. The polarization morphologies of incident VBs are shown for $j = 1$ in (a) and $j = 2$ in (c), and the tightly focused VBs on the focal plane for $j = 1$ in (b) and $j = 2$ in (d). The background color indicates the light intensity $I_r^{\text{in}} = |\mathcal{E}|^2$ and $I_z^{\text{out}} = |E_z|^2$. White and red represent left-handed elliptical and right-handed elliptical polarization states, respectively. In (a) and (b), $m_1 = 2, l_1 = -1, \alpha_1 = \pi$; in (c) and (d), $m_2 = 1, l_2 = 3, \alpha_2 = 0.3\pi$. The spatial distributions of Ω_r and Ω_z are shown in (e) and (f), respectively. The spatial coordinates x and y are in units of trap size $a_0 \equiv \sqrt{\hbar/M\omega}$.

π , the polarization distribution is homogeneous, and the VB corresponds to regular left- or right-circularly polarized light [S19]. After passing through the tightly focusing system, the polarization reverses, as shown in Fig. S2 (b).

For $\alpha \neq 0$ or π , the beam exhibits a superposition of left- and right-circularly polarized components, resulting in a VB with a nonuniform polarization distribution, as shown in Fig. S2 (c). On the focal plane, this polarization distribution becomes more complex, as depicted in Fig. S2 (d). Additionally, the tight-focusing system also reduces spot size and increases intensity. Using these tightly focused VBs to couple atomic pseudospin levels, we obtain the spatial distributions of Ω_r and Ω_z shown in Fig. S2 (e) and (f).

S-5. SPIN TEXTURE

We analyze the spin textures in detail. Distinct from the SOAMC induced by LGBs [S9–S11, S13–S18], our scheme introduces a nonzero Ω_z , resulting in a spatially dependent Zeeman shift term $\Omega_z \sigma_z$, providing an additional tunable degree of freedom. The spatial profile of Ω_z resembles a ring-shaped potential, as illustrated in Fig. S3 (g). The spin-up and spin-down components experience opposing external potentials, leading to a spin-polarized ground state. As α_1 and α_2 varies from 0 to π , the population peak locations shift, altering the density distribution of each spin component, with the positions of maximum population of spin-up or spin-down component labeled in Fig. S3 (g). For $\alpha_1 = \alpha_2 = 0$ or π , the ground state becomes fully polarized with $\langle \sigma_z \rangle = \pm 1$, representing a topologically trivial structure. However, for intermediate values with $0 < |\langle \sigma_z \rangle| < 1$, the spin imbalance between the two spin states decreases. Specifically, for $\alpha_1 = \alpha_2 = 0.37\pi$ and 0.45π , we illustrate the density distributions and relative phases in Fig. S3 (a)-(f). The relative phases in Fig. S3 (c) and (f) show that the ground state exhibits a stable multiply quantized vortex with its quantized circulation to be $2\pi \times 5$.

The corresponding spin textures, as shown in Fig. 3 (c) and (d) of the main text, reveal topologically nontrivial giant skyrmion structures. To calculate the topological charge of skyrmion, we define a normalized complex-valued spinor $\chi = [\chi_\uparrow, \chi_\downarrow]^T = [|\chi_\uparrow|e^{i\xi_\uparrow}, |\chi_\downarrow|e^{i\xi_\downarrow}]^T$, satisfying $|\chi_\uparrow|^2 + |\chi_\downarrow|^2 = 1$. The wave functions can be expressed as $\psi_\sigma = \sqrt{\rho_T} \chi_\sigma$, with total density $\rho_T = |\psi_\uparrow|^2 + |\psi_\downarrow|^2$. The pseudospin density is defined as $\mathbf{S} = \chi^\dagger \vec{\sigma}_P \chi$ with $\vec{\sigma}_P$ the Pauli matrix [S20–S23]. The components of \mathbf{S} are expressed as

$$\begin{aligned}
 S_x &= 2|\chi_\uparrow||\chi_\downarrow| \cos(\xi_\uparrow - \xi_\downarrow), \\
 S_y &= -2|\chi_\uparrow||\chi_\downarrow| \sin(\xi_\uparrow - \xi_\downarrow), \\
 S_z &= |\chi_\uparrow|^2 - |\chi_\downarrow|^2,
 \end{aligned} \tag{S33}$$

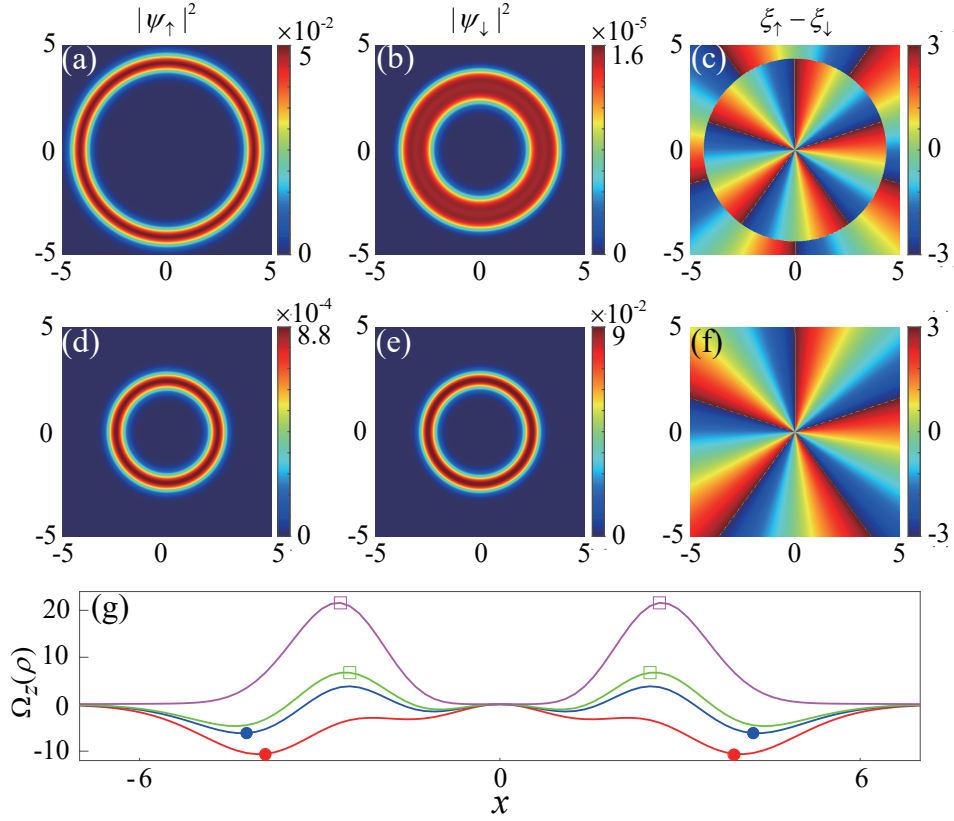


FIG. S3. The ground state density profile $|\psi_\sigma|^2 a_0^2/N$ and relative phase $\xi_\uparrow - \xi_\downarrow$ within the spatial range $x, y \in [-5a_0, 5a_0]$ for different ellipticity angles: (a)-(c) $\alpha_1 = \alpha_2 = 0.37\pi$, (d)-(f) $\alpha_1 = \alpha_2 = 0.45\pi$. (g) The spatial distribution of Ω_z along the x axis at $y = 0$. Red, blue, green, and magenta correspond to $\alpha_1 = \alpha_2 = 0, 0.37\pi, 0.45\pi$, and π , respectively. Circle (square) labels the locations of maximum population of spin-up (spin-down) component. We set the other parameters $\beta_1 = \beta_2 = 0$, $m_1 = 1$, $l_1 = 2$, $m_2 = 1$, $l_2 = -4$, $\delta = 0$, $\Omega_0 = 2.58\hbar\omega$, $\Omega_s = 0$. The coordinates x and y are in units of trap size a_0 .

and $|\mathbf{S}|^2 = S_x^2 + S_y^2 + S_z^2 = 1$. In polar coordinates, the spin vector \mathbf{S} can be written as

$$\mathbf{S} = (\sqrt{1 - S_z^2} \cos(\Delta\kappa\varphi), \sqrt{1 - S_z^2} \sin(\Delta\kappa\varphi), S_z), \quad (\text{S34})$$

where the phases of two spin components can be approximately written as $\xi_\sigma = \kappa_\sigma\varphi$, with $\kappa_\sigma = 0, 1, 2, \dots$ denoting the quantum number of the circulation of the spin component at radius ρ , and $\Delta\kappa = \kappa_\uparrow - \kappa_\downarrow$. For $\alpha_1 = \alpha_2 = 0.37\pi$, $\kappa_\uparrow = 5$, and $\kappa_\downarrow = 0$ at the radii of both the inner and outer annular giant skyrmions. The corresponding topological charge density is written as $q(\rho) = \frac{\Delta\kappa}{4\pi\rho} \frac{dS_z(\rho)}{d\rho}$. Then we find the topological charges of giant skyrmions $Q_{\text{in}} = \int \frac{\Delta\kappa}{4\pi\rho} \frac{dS_z(\rho)}{d\rho} d\rho = (\kappa_\uparrow - \kappa_\downarrow)_{\text{in}} = 5$ and $Q_{\text{out}} = -(\kappa_\uparrow - \kappa_\downarrow)_{\text{out}} = -5$. Increasing α_1 and α_2 to $\alpha_1 = \alpha_2 = 0.45\pi$, we find a single giant skyrmion with topological charge $Q = -5$. Additionally, we perform calculations in the absence of Ω_z , and find topologically trivial spin textures. This shows that the rich topological structures arise from the interplay of Ω_z and Ω_r , demonstrating the high tunability of VB-induced gauge fields in exploring topological quantum phenomena.

-
- [S1] B. Richards and E. Wolf, Proceedings of the Royal Society of London. Series A. Mathematical and Physical Sciences **253**, 358 (1959).
[S2] Z. Chen, L. Hua, and J. Pu, Progress in Optics **57**, 219 (2012).
[S3] P. Yu, Y. Liu, Z. Wang, Y. Li, and L. Gong, Annalen Der Physik **532**, 2000110 (2020).
[S4] F. Le Kien, P. Schneeweiss, and A. Rauschenbeutel, Eur. Phys. J. D **67**, 1 (2013).
[S5] N. Goldman, G. Juzeliūnas, P. Öhberg, and I. B. Spielman, Rep. Prog. Phys. **77**, 126401 (2014).
[S6] H. Zhai, Reports on Progress in Physics **78**, 026001 (2015).
[S7] H. Zhai, *Ultracold atomic physics* (Cambridge University Press, Cambridge, England, 2021).
[S8] K.-J. Chen, F. Wu, S.-G. Peng, W. Yi, and L. He, Physical Review Letters **125**, 260407 (2020).

- [S9] D. Zhang, T. Gao, P. Zou, L. Kong, R. Li, X. Shen, X.-L. Chen, S.-G. Peng, M. Zhan, H. Pu, et al., *Physical Review Letters* **122**, 110402 (2019).
- [S10] H.-R. Chen, K.-Y. Lin, P.-K. Chen, N.-C. Chiu, J.-B. Wang, C.-A. Chen, P. Huang, S.-K. Yip, Y. Kawaguchi, and Y.-J. Lin, *Physical Review Letters* **121**, 113204 (2018).
- [S11] C. Qu, K. Sun, and C. Zhang, *Physical Review A* **91**, 053630 (2015).
- [S12] C. J. Pethick and H. Smith, *Bose-Einstein condensation in dilute gases* (Cambridge University Press, Cambridge, England, 2018), 2nd ed.
- [S13] M. DeMarco and H. Pu, *Physical Review A* **91**, 033630 (2015).
- [S14] K. Sun, C. Qu, and C. Zhang, *Physical Review A* **91**, 063627 (2015).
- [S15] Y.-X. Hu, C. Miniatura, and B. Gremaud, *Physical Review A* **92**, 033615 (2015).
- [S16] L. Chen, H. Pu, and Y. Zhang, *Physical Review A* **93**, 013629 (2016).
- [S17] L. Chen, Y. Zhang, and H. Pu, *Physical Review Letters* **125**, 195303 (2020).
- [S18] S.-G. Peng, K. Jiang, X.-L. Chen, K.-J. Chen, P. Zou, and L. He, *AAPPS Bulletin* **32**, 36 (2022).
- [S19] C. Rosales-Guzmán, B. Ndagano, and A. Forbes, *Journal of Optics* **20**, 123001 (2018).
- [S20] H. Wang, L. Wen, H. Yang, C. Shi, and J. Li, *Journal of Physics B: Atomic, Molecular and Optical Physics* **50**, 155301 (2017).
- [S21] J. Jin, S. Zhang, W. Han, and Z. Wei, *Journal of Physics B: Atomic, Molecular and Optical Physics* **46**, 075302 (2013).
- [S22] S.-J. Yang, Q.-S. Wu, S.-N. Zhang, and S. Feng, *Physical Review A—Atomic, Molecular, and Optical Physics* **77**, 033621 (2008).
- [S23] X. Su, W. Dai, T. Li, J. Wang, and L. Wen, *Chaos, Solitons & Fractals* **184**, 114979 (2024).